Three-body fragmentation dynamics of $BrCN^{q+}$ ($q = 3$–6) induced by 1-keV electron impact

Wenchao Zhao, Enliang Wang,* Lei Chen, Xu Shan,† and Xiangjun Chen
Hefei National Research Center for Physical Sciences at the Microscale and Department of Modern Physics, University of Science and Technology of China, Hefei 230026, China

(Received 3 February 2023; revised 19 April 2023; accepted 8 May 2023; published 30 May 2023)

The three-body fragmentation dynamics of $BrCN^{q+}$ ($q = 3$–6) produced by 1-keV electron impact has been investigated using the ion momentum imaging technique. Up to 11 three-body Coulomb explosion channels were identified and analyzed. The corresponding kinetic energy release (KER) distributions were obtained and compared with the predictions of the Coulomb explosion model. By means of the Dalitz plot, Newton diagram, and native frame method, we have studied the concerted and sequential fragmentation mechanisms for channels leading to $Br^{l+} + C^+ + N^+$ ($l = 1$–3). The KER for the intermediate dications BrC^{2+} and CN^{2+} from the sequential mechanism were determined and the electronic states of the intermediate molecular ion CN^{2+} were discussed. For the channels leading to higher charge states of the carbon and nitrogen ions, only the concerted fragmentation mechanism was observed.

DOI: 10.1103/PhysRevA.107.052811

I. INTRODUCTION

The fragmentation dynamics of multiply charged polyatomic molecules has attracted much attention over the past few decades due to its importance in a wide range of areas, such as planetary atmospheric chemistry [1,2], plasma physics [3–6], and radiation damage of biological tissues [7–14]. The multiply charged molecular ions can be generated by photon absorption [15–19], electron impact [20–24], highly charged ion impact [25–34], and intense laser field ionization [35–39]. Driven by the strong repulsive potential, the multiply charged molecules will decay via various pathways which are described by the Coulomb explosion model. In previous studies [26,40], it has been found that the three-body fragmentation of polyatomic molecular ions can proceed through a concerted or sequential mechanism depending on whether a metastable intermediate is formed. For the concerted fragmentation mechanism, the chemical bonds are broken simultaneously, while in the case of sequential mechanism, the previous studies showed that it happens in the low-lying electronic states where the intermediate is weakly bounded [26] and can be broken due to the influence of the first ejected ion.

The identification and elucidation of the fragmentation processes of polyatomic molecules are important for the understanding of multibody quantum correlation dynamics. During the past decades, the development of multiple coincidence ion momenta imaging techniques, such as the recoil ion momentum spectrometer [41,42], cold target recoil ion momentum spectroscopy (COLTRIMS) or the reaction microscope [43–45], and the velocity map imaging (VMI) technique [46], made it feasible to detect all the fragment ions and reconstruct their three-dimensional momentum vectors. In consequence, the kinetic energy release (KER) and the momentum correlation between the fragment ions can be determined. For the three-body fragmentations, the Dalitz plots [47,48], Newton diagrams [16], and the native frames method [49,50] have been proven to be powerful tools to provide insight into the multibody quantum correlations. Until now, a variety of molecules, including the symmetric triatomic molecules CO_2 [26,40,51–54], CS_2 [23], and H_2O [55], and the asymmetric triatomic molecules N_2O [56,57] and OCS [15,22,31,49,50], have been investigated by electron collision [22,23,53–56], ion collision [26,31,40,50,52,57], and photon absorption [15,49,51].

Cyanogen bromide (BrCN) could be a previously unquantified participant in active Br chemistry which has been suggested to play an important role in ozone loss. The dissociation of BrCN is one of the sources of the active bromine which participates in the destruction of ozone. Therefore, BrCN is important for understanding the cycle of activated bromine [58]. Until now, the dynamics of the dissociative electron attachment [59–61] and electron-induced ion-pair dissociation [62] of BrCN have been studied. To the best of our knowledge, the investigation of the dissociation dynamics of highly charged BrCN is still scarce. In the present work, the three-body fragmentation dynamics of $BrCN^{q+}$ ($q = 3$–6) induced by 1-keV electron impact was studied using an ion momentum imaging spectrometer. Eleven three-body dissociation channels were identified and their KER distributions were obtained. By means of the Dalitz plot, Newton diagram, and native frame method, the concerted and sequential fragmentation mechanisms of the $Br^{l+} + C^+ + N^+$ ($l = 1$–3) channels were identified and discriminated. For channels that end up with higher charge states such as N^{2+} or C^{2+}, only the concerted fragmentation mechanism was observed. The obtained KERs of the concerted channels were compared with the predictions of the Coulomb explosion model.

*elwang@ustc.edu.cn
†xshan@ustc.edu.cn

II. EXPERIMENT

The experiment was performed using an ion momentum imaging spectrometer which has been described in detail elsewhere [24]. In brief, the powder sample BrCN was purchased from J&K Scientific with a purity of 98%. The vapor pressure of BrCN is 13.3 kPa and can be volatilized to gas phase at room temperature. The gas-phase BrCN was effused from a capillary. In the interaction region (approximately $1 \times 1 \times 2\,\mathrm{mm}^3$), the gas-phase target collided with electrons emitted from a tantalum cathode illuminated by the 266-nm laser pulse. The pulse width and repetition frequency are 600 ps and 20 kHz, respectively. The created fragment ions were extracted by a pulsed electrostatic field of 50 V/cm which was switched on after the electron beam exiting the interaction region. After passing through the acceleration region of 50 mm and a field-free drift tube of 100 mm, the ions were detected by a temporal- and position-sensitive detector (PSD). The three-dimensional (3D) momentum vectors of ions were reconstructed from the time-of-flight (TOF) and position signals. In the present work, the background pressure is lower than 5.0×10^{-7} Pa and the working pressure is about 2×10^{-5} Pa. The incident electron energy and average current were 1.0 keV and 40.0 pA, respectively. To improve the efficiency, only the events with at least two fragment ions were recorded for the online data acquisition.

For three-body dissociative channels, the Dalitz plots, Newton diagrams, and native frame methods are employed to elucidate the fragmentation mechanisms. The Dalitz plot provides a powerful analytic tool to visualize the momentum vector correlations and identify the fragmentation mechanisms. In the Dalitz plot, the data are placed inside a circle of radius $\frac{1}{3}$ inscribed in an equilateral triangle. The perpendicular distances from one specific point inside the plot to the edges are defined as ε_i, which are the normalized squared momentum of the three fragments,

$$\varepsilon_i = \frac{p_i^2}{\sum_{j=1}^{3} p_j^2}, \tag{1}$$

where p_i is the momentum of the ith ($i = 1, 2, 3$) fragment ion. The Cartesian coordinates x and y of the Dalitz plot are defined as

$$x = \frac{\varepsilon_1 - \varepsilon_2}{\sqrt{3}}, \tag{2}$$

$$y = \varepsilon_3 - \frac{1}{3}. \tag{3}$$

As shown in Fig. 1, each point in the Dalitz plot represents a specific momentum correlation pattern of the three fragments. Usually, the localized events in the Dalitz plot correspond to the concerted fragmentation process while the delocalized events scattering along a certain curve originate from the sequential fragmentation process.

In the Newton diagram, the x axis is defined by the momentum vector of one fragment. The other two fragments are placed in the upper and lower halves of the diagram. In this work, the momenta of the three fragments are normalized by the one on the x axis. The previous studies showed that, in addition to the localized distributions from the concerted fragmentation, sequential fragmentation presents

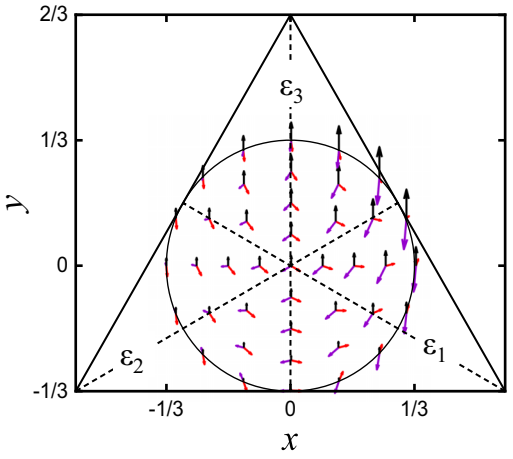

FIG. 1. Definition of the Dalitz plot. The arrows at each point show the momentum correlation of the three fragments.

circular structures due to the rotation of the intermediate moiety relative to the first emitted fragment. Usually, there are overlaps between the distributions of concerted and sequential fragmentation in the Newton diagram. The native frame method allows for separating the sequential and concerted processes taking advantage of the rotation of the intermediate molecular fragment [49,50]. The detailed definition of the native frame method will be shown when we discuss the three-body dynamics in the following. Briefly, if the lifetime of the intermediate molecule fragment is longer than its rotation period in the sequential fragmentation, the metastable moiety has enough time to rotate at least one period and the KER from this moiety will be independent of the rotation angle relative to the first emitted ion. In the case of the concerted fragmentation, the molecule dissociates without intermediate moiety rotation. The two mechanisms can be separated with the help of the rotation angle versus the KER spectrum of the intermediate molecule in which a uniform angular distribution corresponds to the sequential fragmentation.

III. RESULTS AND DISCUSSION

A. Ion coincidence maps and identification of the fragmentation channels

The TOF spectrum of BrCN impact by 1.0 keV electrons is shown in Fig. 2(a). Due to the comparable abundance of the isotopes of bromine (the abundance ratio of ^{79}Br:^{81}Br is 100:97.3), two intense sharp peaks are observed for the parent ions. Charge states up to 2 are observed for the fragment ions. Due to the high kinetic energy acquired in the Coulomb explosion process, the TOF of fragment ions has a broad distribution, resulting in an overlap between them. At a TOF of about 5.2 and 7.3 μs, the sharp peaks indicate possible contaminations of $C_2N_2^+$ and $C_2N_2^{2+}$ due to the impurity N≡C−C≡N in the sample. But these ions can be filtered out by applying the TOF correlations and momentum conservation.

Figure 2(b) shows the ion1+ion2-ion3 coincidence map for the fragment ions from the three-body fragmentation channels of $BrCN^{q+}$ ($q = 3$–6). In this map, the horizontal axis is the sum of the TOFs of the first and the second detected ions and the vertical axis is the TOF of the third one. Under the

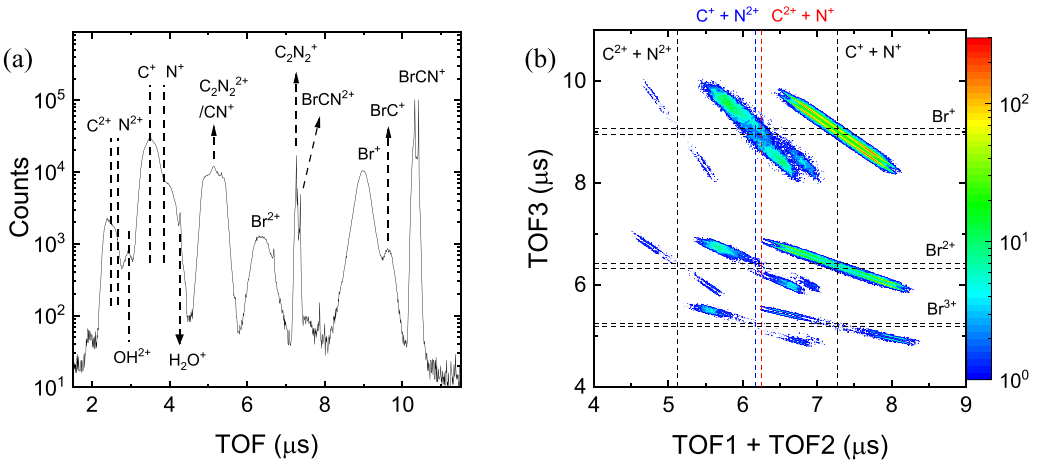

FIG. 2. (a) One-dimensional TOF spectrum of the first hit ions; (b) ion1+ion2-ion3 coincidence map for the fragment ions of $BrCN^{q+}$ ($q = 3$–6). Here, the bromine ions contain two isotopes, ^{79}Br and ^{81}Br.

present experimental conditions, the ions with perpendicular kinetic energy higher than 15 eV were lost due to the limited strength of the extraction field. This leads to the lack of counts in the middle of the islands. The obtained kinetic energy of the ions emitted toward and backward from the detector within a 30° solid angle (a cone with the same axis as the TOF axis and its apex at the center of the collision area, and with its half apex angle equal to 15°) was compared with that without angular condition restriction and no significant difference was found. Hence, the influence of the incomplete collection efficiency on the KER distribution is negligible. This is because the molecules are randomly oriented during the impact ionization. Thereby the final kinetic energy of the ions is independent of the emission angle. The lost ions emitting perpendicular to the TOF axis only lower the total counts of a specific channel rather than changing the kinetic energy distributions. To ensure that the incomplete collection has no influence, the emission angular condition restriction

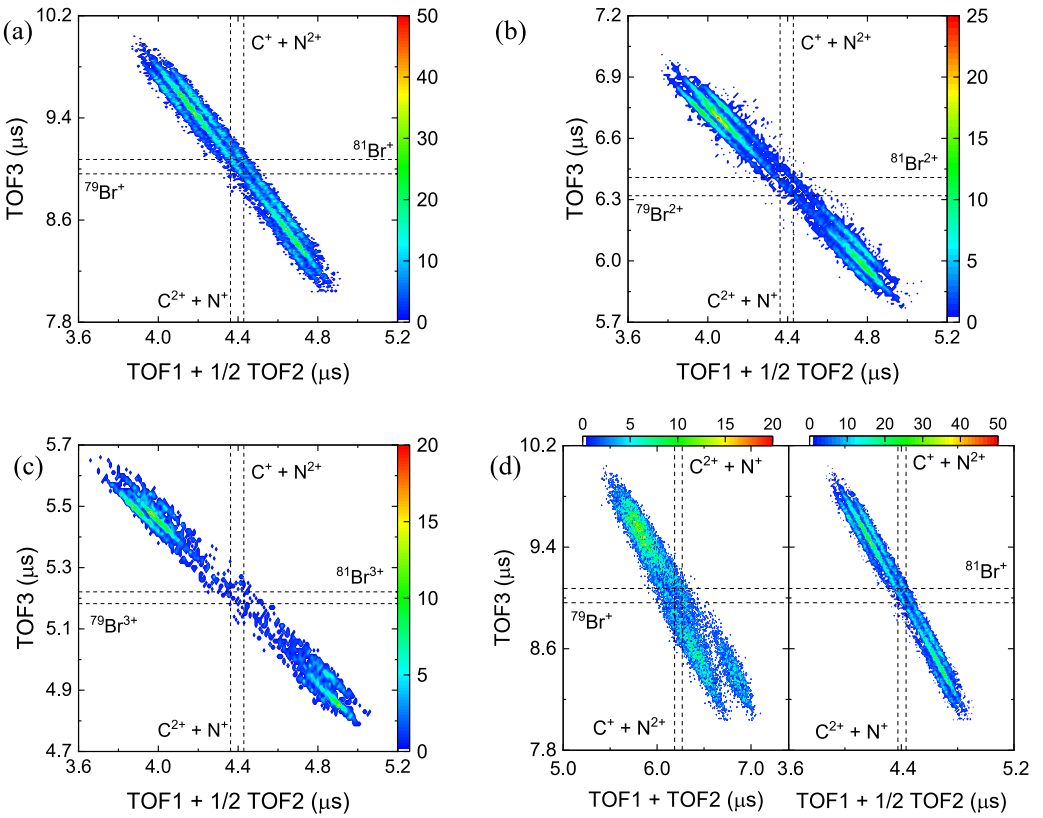

FIG. 3. (a)–(c) The coincidence maps of TOF3 versus TOF1 + $(q2/q1)$TOF2 for the $Br^{l+} + C^{2+} + N^{+}$ and $Br^{l+} + C^{+} + N^{2+}$ ($l = 1$–3) channels, respectively. (d) The ion1+ion2-ion3 coincidence map and the coincidence map of TOF3 versus TOF1 + $(q2/q1)$TOF2 for the $Br^{+} + C^{2+} + N^{+}$ and $Br^{+} + C^{+} + N^{2+}$ channels.

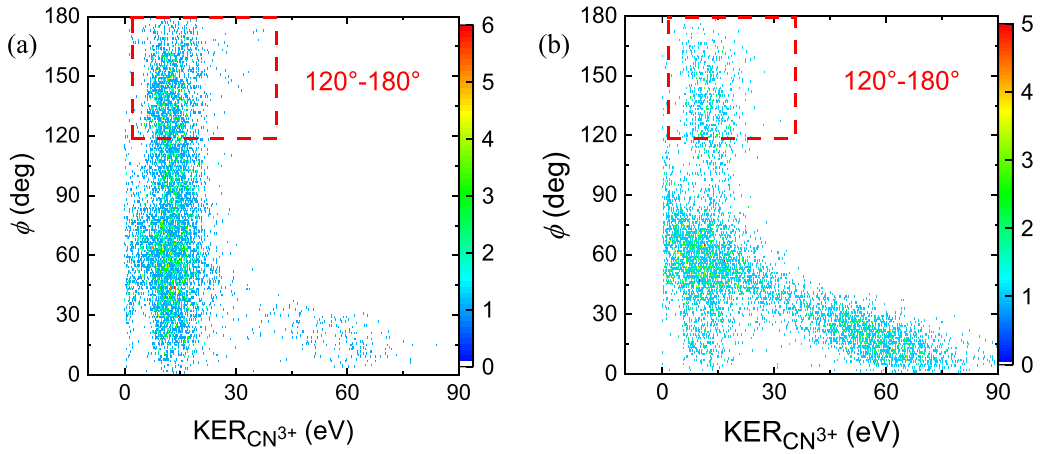

FIG. 4. (a) $KER_{CN^{3+}} - \phi$ plot by assuming the channel to be $^{79}Br^{+} + C^{+} + N^{2+}$. (b) $KER_{CN^{3+}} - \phi$ plot by assuming the channel to be $^{81}Br^{+} + C^{2+} + N^{+}$.

($\pm 30^{\circ}$ solid angle) is applied in extracting the branching ratios. Due to the comparable abundance isotopes, each of the three-body fragmentation channels consists of a pair of coincidences. As shown in Fig. 2(b), except for the channels with $C^{2+} + N^{+}$ and $C^{+} + N^{2+}$ coincidences (marked by the dashed blue and red lines), other channels can be accurately identified using the ion1+ion2-ion3 coincidence map. For the $Br^{l+} + C^{2+} + N^{+}$ and $Br^{l+} + C^{+} + N^{2+}$ ($l = 1$–3) channels, the coincidence islands are obscured due to the unequal charge states of the first and second hit ions (C^{2+}/N^{+} or N^{2+}/C^{+} coincidence). Recently, a charge-encoded multiphotoion coincidence (cMUPICO) method [63,64] was proposed for distinguishing various dissociation channels in which charge states of the ionic fragment are considered. In brief, the horizontal axis of the coincidence map becomes TOF1 + $(q2/q1)$TOF2 instead of the sum TOFs, where $q1$ and $q2$ are charge states of the first and the second ions, respectively. Following this method, the events of the the $Br^{l+} + C^{2+} + N^{+}$ and $Br^{l+} + C^{+} + N^{2+}$ ($l = 1$–3) channels are plotted on a coincidence map of TOF3 versus TOF1 + $(q2/q1)$TOF2 with a charge ratio of 1:2 for $q2/q1$. The results are shown in Figs. 3(a)–3(c) for the channels with Br^{+}, Br^{2+}, and Br^{3+}, respectively. The improvement is clearly shown in Fig. 3(d) by comparing the standard TOF correlation map and the cMUPICO spectrum of the $Br^{+} + C^{2+} + N^{+}$ and $Br^{+} + C^{+} + N^{2+}$ channels. The bottom and the top coincidence islands can be assigned unambiguously in Figs. 3(a)–3(c). The islands at the centers contain two channels, i.e., $^{79}Br^{l+} + C^{+} + N^{2+}$ and $^{81}Br^{l+} + C^{2+} + N^{+}$ where $l = 1$, 2, and 3 in Figs. 3(a)–3(c), respectively.

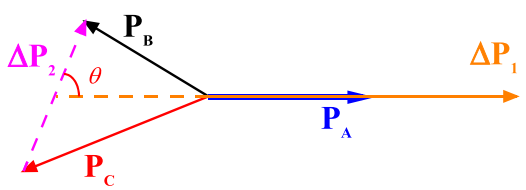

FIG. 5. Schematic of the kinematics of the sequential dissociation channel ABC → A + BC → A + B + C.

The overlapped channels at the center in Figs. 3(a)–3(c) are further separated as follows: the random orientation of the target molecules ensures an isotropic angular distribution of the ion. Hence, the KER distribution of the fragmentation channel is independent of the dissociation angle. Here, we take the momenta of carbon and nitrogen ions. The relative momentum vector is defined by $\Delta p = (m_N p_C - m_C p_N)/(m_C + m_N)$ where m_C and m_N are the mass of the carbon and nitrogen ions, respectively; p_C and p_N are the measured momenta of the carbon and nitrogen ions, respectively. We define the reduced KER_{CN} and ion ejection angle ϕ, where $KER_{CN^{3+}} = (\Delta p)^2/2\mu_{CN}$ with μ_{CN} being the reduced mass of the carbon and nitrogen ions, and ϕ is the angle between the Δp and the extraction field (z axis). Based on the fact that the KER is independent of the dissociation angle, if we plot a $KER_{CN^{3+}} - \phi$ map, the events of the correctly identified channels should be distributed on a vertical line. Figure 4(a) shows the $KER_{CN^{3+}} - \phi$ plot of the events that correspond to the middle coincidence island in Fig. 3(a) by assuming all of them come from the $^{79}Br^{+} + C^{+} + N^{2+}$ channel while the same events are shown in Fig. 4(b) assuming the channel to be $^{81}Br^{+} + C^{2+} + N^{+}$. Two distinct structures can be observed in these plots. In Fig. 4(a), one structure extends from 0° to 180° and its $KER_{CN^{3+}}$ is independent of ϕ, which can be assigned to the $^{79}Br^{+} + C^{+} + N^{2+}$ channel. For the bottom structure of the plot, the $KER_{CN^{3+}}$ varies with ϕ which is in contradiction with the fact that the KER is independent of the dissociation angle. The events located in this area come from the $^{81}Br^{+} + C^{2+} + N^{+}$ channel whose $KER_{CN^{3+}} - \phi$ map is shown in Fig. 4(b). To avoid overlaps, we choose the events within $\phi \in [120^{\circ}, 180^{\circ}]$ both in Figs. 4(a) and 4(b) to extract the channels. As for the $^{79}Br^{l+} + C^{+} + N^{2+}$ and $^{81}Br^{l+} + C^{2+} + N^{+}$ ($l = 2$, 3) channels, the same method is applied to assign and extract the events.

In the offline analysis, the results of the ^{79}Br and ^{81}Br channels are identical. Therefore, the sum of them is presented in this work to have better statistics. The KERs and the momentum correlation angles (MCAs) of the concerted process for these three-body fragmentation channels of $BrCN^{q+}$ ($q = 3$–6) are summarized in Table I. The MCA α

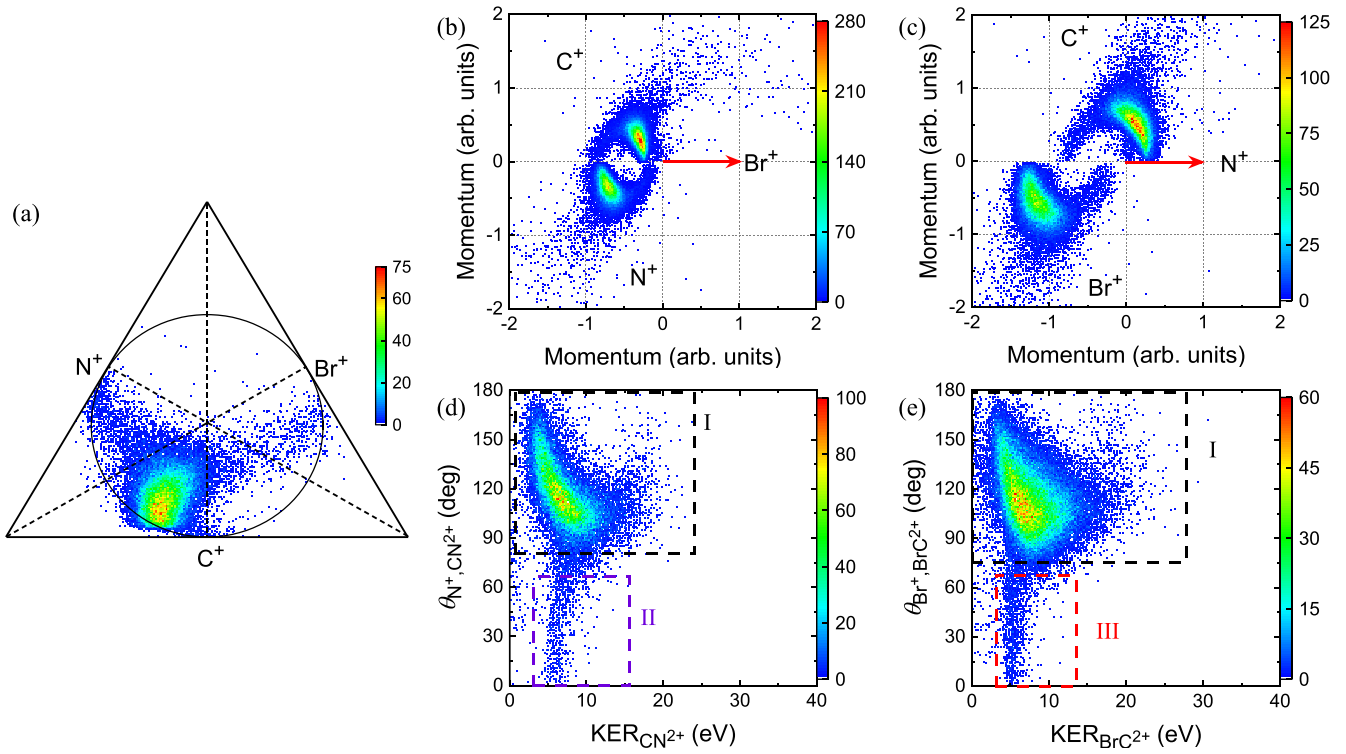

FIG. 6. Experimental results for the $Br^+ + C^+ + N^+$ channel. (a) Dalitz plot; (b), (c) Newton diagrams with Br^+ and N^+ as references. (d) Native frame plot assuming sequential breakup of $BrCN^{3+}$ with CN^{2+} as the molecular intermediate. (e) Native frame plot assuming sequential breakup of $BrCN^{3+}$ with BrC^{2+} as the molecular intermediate. The events in region I of (d,e) are from the concerted process $BrCN^{3+} \rightarrow Br^+ + C^+ + N^+$, and the regions II in (d) and III in (e) correspond to sequential processes $BrCN^{3+} \rightarrow Br^+ + CN^{2+} \rightarrow Br^+ + C^+ + N^+$ and $BrCN^{3+} \rightarrow BrC^{2+} + N^+ \rightarrow Br^+ + C^+ + N^+$, respectively.

is obtained by the momentum vectors of two associated ions, p_1 and p_2,

$$\alpha = \arccos\left(\frac{p_1 \cdot p_2}{|p_1||p_2|}\right). \tag{4}$$

TABLE I. The KERs and the MCAs of the concerted process for three-body fragmentation channels of $BrCN^{q+}$ (q = 3–6).

	KER (eV)		MCA (deg)	
Channels	Experimental	CE[a]	$p_{Br} - p_C$[b]	$p_{Br} - p_N$[c]
$Br^+ + C^+ + N^+$	20.5	24.9	130	152
$Br^{2+} + C^+ + N^+$	33.0	37.6	140	156
$Br^{3+} + C^+ + N^+$	43.0	50.3	144	160
$Br^+ + C^{2+} + N^+$	40.5	45.0	134	151
$Br^{2+} + C^{2+} + N^+$	53.0	65.6	140	152
$Br^{3+} + C^{2+} + N^+$	63.0	86.2	144	154
$Br^+ + C^+ + N^{2+}$	36.0	41.9	124	156
$Br^{2+} + C^+ + N^{2+}$	51.0	59.4	132	160
$Br^{3+} + C^+ + N^{2+}$	61.0	76.9	140	162
$Br^+ + C^{2+} + N^{2+}$	57.0	74.2	125	152
$Br^{2+} + C^{2+} + N^{2+}$	72.0	99.6	132	154

[a]The prediction from the Coulomb explosion model.
[b]Momentum correlation angle between bromine and carbon ions.
[c]Momentum correlation angle between bromine and nitrogen ions.

At the end of the sections, the differences between the experimental KER and the predictions by the Coulomb explosion (CE) model will be discussed.

B. Concerted and sequential fragmentation dynamics for $Br^{l+} + C^+ + N^+$ (l = 1–3) channels

The Dalitz plot of the $Br^+ + C^+ + N^+$ channel is shown in Fig. 5(a). The plot demonstrates an intense area near the left bottom and two winglike structures extending from the intense area to both side edges. The intense area corresponds to the concerted fragmentation where the carbon shares the lowest kinetic energy. The left and right halves of the winglike structures originate from the sequential dissociation of $BrCN^{3+}$ via the intermediate molecular ions CN^{2+} and BrC^{2+}, respectively. The Newton diagrams of this channel are presented in Figs. 5(b) and 5(c) where the momenta of the ions are normalized to that of Br^+ and N^+, respectively. Both of these Newton diagrams show two intense spots and a clear circular structure. The two spots in the Newton diagram correspond to the intense area in the Dalitz plot, i.e., the concerted fragmentation. The circular structure, which is due to the rotation of the intermediate molecular ion CN^{2+} or BrC^{2+}, is a sign of the sequential fragmentation process. There are overlaps between the events from concerted and sequential fragmentation. To discriminate the events from the two mechanisms, the native frame method is adopted. Assuming the channel to be $ABC \rightarrow A + BC \rightarrow A + B + C$ as schematically shown in

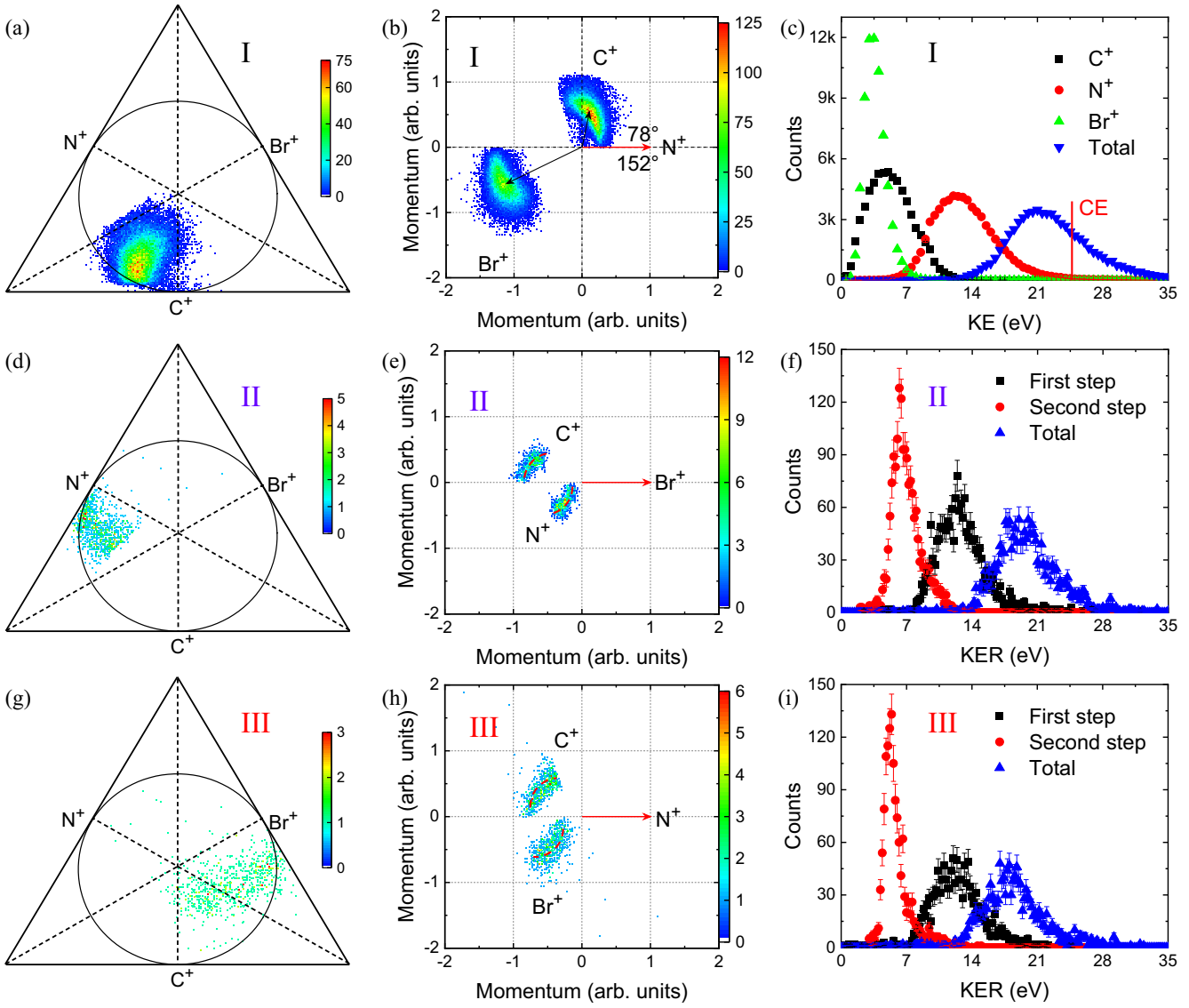

FIG. 7. (a)–(c) Dalitz plot, Newton diagram, and KER distributions for region I in Figs. 6(d) and 6(e). (d)–(f) Dalitz plot, Newton diagram, and KER distributions for region II in Fig. 6(d). (g)–(i) Dalitz plot, Newton diagram, and KER distributions for region III in Fig. 6(e). The angles on the upper and lower halves of the Newton diagrams in (b) are MCAs between the N^+ ion and C^+ ion, and the N^+ ion and Br^+ ions, respectively. Red solid line in (c) represents the KER predicted by the CE model. The first step and second step in (f) represent the KER of $BrCN^{3+} \rightarrow Br^+ + CN^{2+}$ and $CN^{2+} \rightarrow C^+ + N^+$, respectively, and "Total" represents the sum of the two steps. The first step and second step in (i) represent the KERs of $BrCN^{3+} \rightarrow N^+ + BrC^{2+}$ and $BrC^{2+} \rightarrow C^+ + Br^+$, respectively, and "Total" represents the sum of the two steps.

Fig. 5, we plotted the density plots of the events as a function of relative angle θ and KER, where KER is the kinetic energy released by the intermediate in the second step and θ is defined as the angle between the momentum of A and BC in the native frame [65]

$$\theta = \arccos\left(\frac{\Delta\mathbf{P}_1 \cdot \Delta\mathbf{P}_2}{|\Delta\mathbf{P}_1||\Delta\mathbf{P}_2|}\right), \tag{5}$$

where $\Delta\mathbf{P}_1$ and $\Delta\mathbf{P}_2$ are expressed as

$$\Delta\mathbf{P}_1 = \frac{m_B + m_C}{m_A + m_B + m_C}\mathbf{P}_A - \frac{m_A}{m_A + m_B + m_C}(\mathbf{P}_B + \mathbf{P}_C), \tag{6}$$

$$\Delta\mathbf{P}_2 = \frac{m_C}{m_B + m_C}\mathbf{P}_B - \frac{m_B}{m_B + m_C}\mathbf{P}_C. \tag{7}$$

Here, $\mathbf{P}_A$, $\mathbf{P}_B$, and $\mathbf{P}_C$ are measured momentum vectors of A, B, and C, respectively. m_A, m_B, and m_C are the mass of three fragments A, B, and C, respectively.

The native frame plots assuming sequential breakup of $BrCN^{3+}$, CN^{2+} and BrC^{2+} being the intermediates, are shown in Figs. 6(d) and 6(e), respectively. Uniform angular distributions are observed in both native frame plots between 0° and 70° which are clearly separated from the intense areas from the concerted fragmentation. To show the momentum correlations and KER distributions of the specific mechanisms, we extract the events from concerted fragmentation by applying the conditions marked by area I in Figs. 6(d) and 6(e). The events from the sequential fragmentation with CN^{2+} and BrC^{2+} as the intermediate moieties are marked by areas II in Fig. 6(d) and III in Fig. 6(e), respectively. The Dalitz plots,

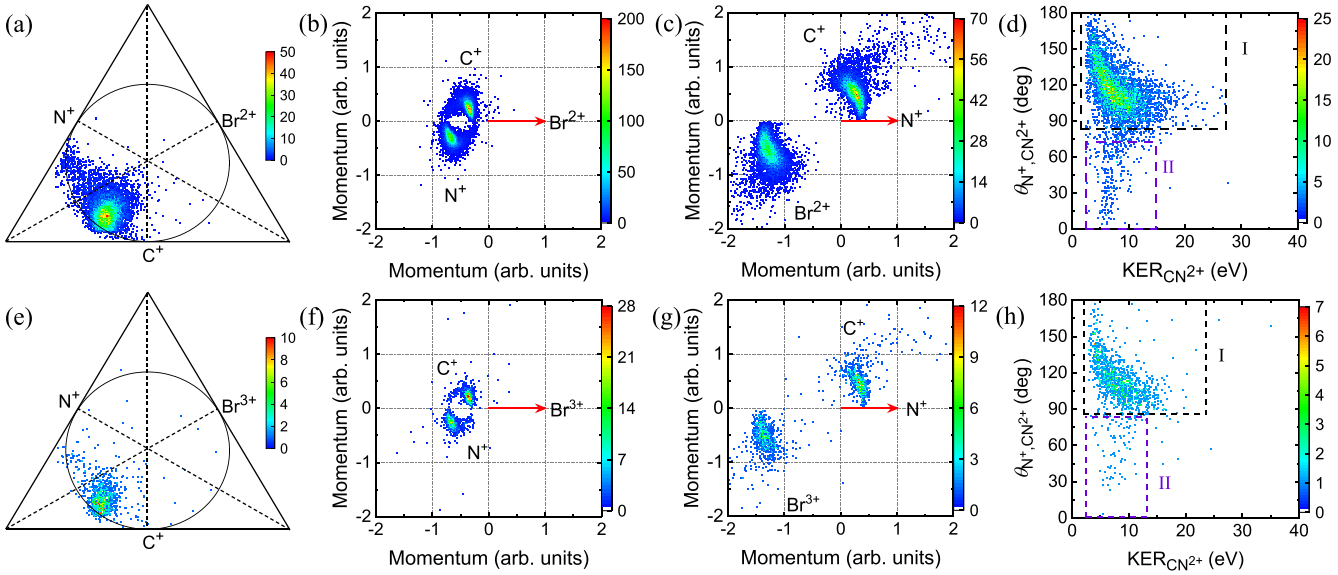

FIG. 8. The Dalitz plot, Newton diagrams with Br ion and N ion as references, and native frame plot for the $Br^{2+} + C^+ + N^+$ channel in (a)–(d), respectively, and for the $Br^{3+} + C^+ + N^+$ channel in (e)–(h), respectively. The events in regions I and II of (d) are generated via the concerted process $BrCN^{4+} \rightarrow Br^{2+} + C^+ + N^+$ and the sequential processes $BrCN^{4+} \rightarrow Br^{2+} + CN^{2+} \rightarrow Br^{2+} + C^+ + N^+$, respectively. The events in regions I and II of (h) are generated via the concerted process $BrCN^{5+} \rightarrow Br^{3+} + C^+ + N^+$ and the sequential processes $BrCN^{5+} \rightarrow Br^{3+} + CN^{2+} \rightarrow Br^{3+} + C^+ + N^+$, respectively.

Newton diagrams, and KER distributions for the three regions are exhibited in Fig. 7.

The Dalitz plot, Newton diagram, and kinetic energy distributions of the concerted fragmentation of the $Br^+ + C^+ + N^+$ channel are shown in Figs. 7(a)–7(c). The intense area near the edge (C^+) in the Dalitz plot and two intense islands in the Newton diagram confirm that the events in region I of Figs. 6(d) and 6(e) originate from a concerted fragmentation mechanism. For the concerted breakup process, the most probable MCAs between the Br^+ and the N^+ ions, and between the Br^+ and the C^+, ions are 152° and 130°, respectively. The range of the KER of the concerted breakup process is from 13 to 35 eV with a peak at about 20.5 eV. The branching ratio of the concerted breakup process is 93.5% ± 1.6%. The uncertainty only includes the statistical error.

The Dalitz plot and Newton diagram for region II in Fig. 6(d) are displayed in Figs. 7(d) and 7(e), respectively. The left-winglike structure extending from the bottom edge (C^+) to the left edge (N^+) in the Dalitz plot and the circular structure in the Newton diagrams confirm the sequential dissociation process, i.e., $BrCN^{3+} \rightarrow Br^+ + CN^{2+} \rightarrow Br^+ + C^+ + N^+$. The KER distributions for the first and second steps of the sequential fragmentation and the sum of the final three ions are shown in Fig. 7(f). The total KER distribution ranges from about 13 to 27 eV with the most probable value at about 19 eV. Similar to the previous studies, the KER of sequential fragmentation is lower than that of the concerted mechanism; i.e., the sequential mechanism comes from the low-lying electronic states of the molecular ions. The KER distribution in the first step extends from about 7 to 20 eV with a peak value of about 12.4 eV, and the KER distribution in the second step ranges from 3 to 12 eV with a peak value of 6.2 eV. According to the potential energy curves of the electronic states of CN^{2+} as a function of the C-N internuclear distance calculated by the multireference configuration interaction (MRCI) method [66,67], there exists a conical intersection between the $1\,^4\Pi$ and $1\,^2\Delta$ states when the C-N bond length is ∼2.38 bohrs due to the spin-orbital interaction. The theoretical KER of this fragmentation pathway is 6.1 eV, which agrees with the experimental result. The branching ratio for this fragmentation process is 2.5% ± 0.7%.

Figures 7(g)–7(i) depict the Dalitz plot, Newton diagram, and KER distributions for the sequential pathway of $BrCN^{3+} \rightarrow N^+ + BrC^{2+} \rightarrow Br^+ + C^+ + N^+$, which is marked in region III in Fig. 6(e). One can note the right-winglike structure extending from the bottom edge (C^+) to the right edge (N^+) in the Dalitz plot, and a circular structure in the Newton diagram; these confirm the sequential dissociation mechanism. The total KER distributes from about 12 to 25 eV with the most probable value at about 17.5 eV. The KER distribution for the first step ranges from about 7 to 19 eV with the most probable value at about 11.5 eV. The KER distribution for the second step ranges from 3 to 11 eV with a peak value of about 5 eV. The branching ratio of this sequential process is 3.9% ± 0.9%.

The Dalitz plot, Newton diagrams with bromine ion and nitrogen ion as references, and native frame plot for the $Br^{2+} + C^+ + N^+$ channel are displayed in Figs. 8(a)–8(d), respectively. The corresponding diagrams for the $Br^{3+} + C^+ + N^+$ channel are displayed in Figs. 8(e)–8(h), respectively. Different from the $Br^+ + C^+ + N^+$ channel, only intense areas near the bottom edge of the triangle (C^+) and left-winglike structures extending from the bottom edge (C^+) to the left edge

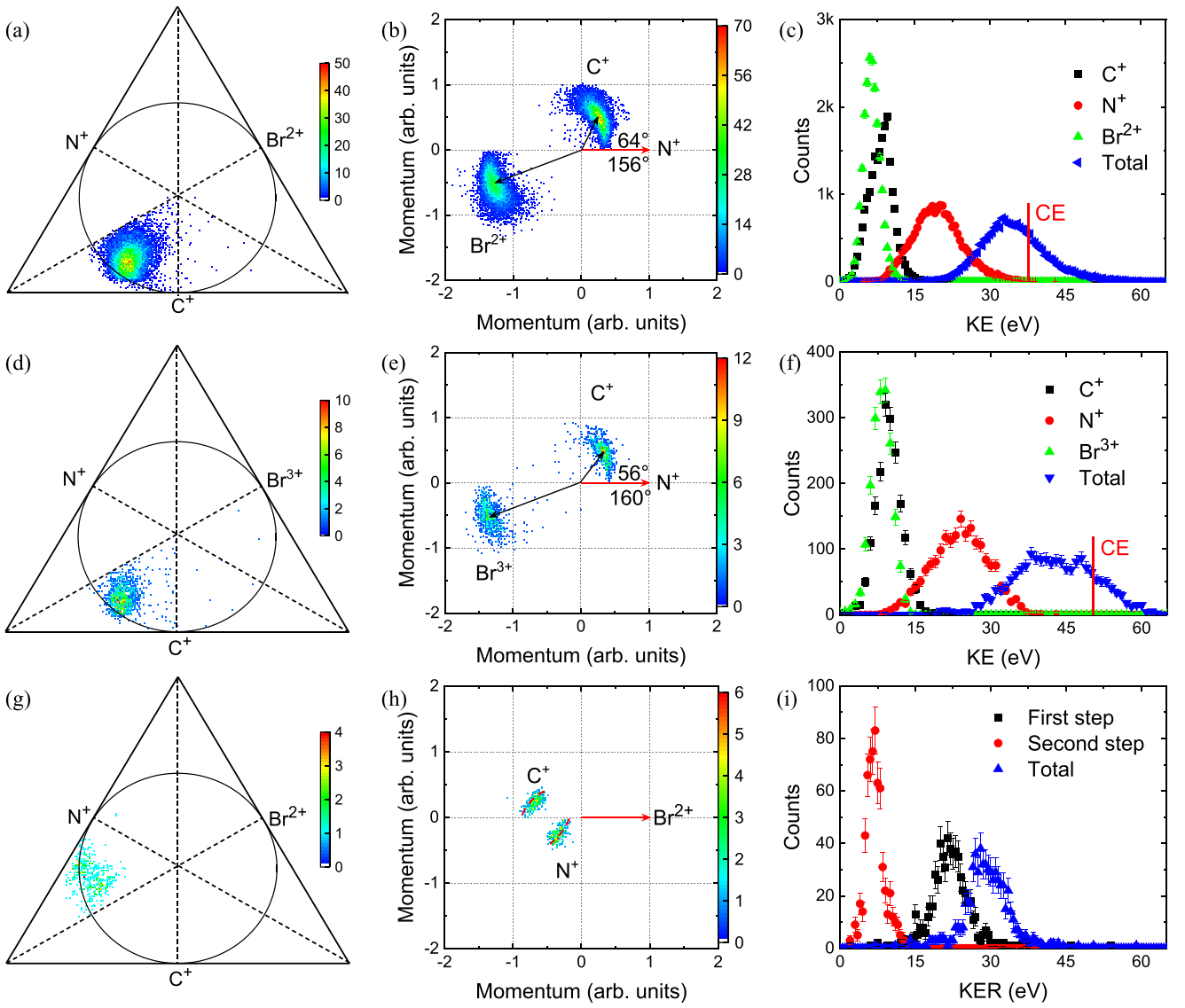

FIG. 9. Dalitz plot, Newton diagram, and KER distributions for the concerted fragmentation of $Br^{2+} + C^+ + N^+$ in (a)–(c), respectively, for the concerted fragmentation of $Br^{3+} + C^+ + N^+$ in (d)–(f), respectively, and for the sequential fragmentation of $Br^{2+} + C^+ + N^+$ in (g)–(i), respectively. The angles on the upper and lower halves of the Newton diagrams in (b), (e) are MCAs between the N^+ ion and C^+ ion, and those between the N^+ ion and Br^{2+}/Br^{3+} ions, respectively. Red solid lines in (c), (f) represent the KERs predicted by the CE model. The first and second steps in (i) represent the KERs of $BrCN^{4+} \rightarrow Br^{2+} + CN^{2+}$ and $CN^{2+} \rightarrow C^+ + N^+$, respectively, and "Total" represents the sum of the two steps.

(N^+) are observed in the Dalitz plots, as shown in Figs. 8(a) and 8(e). These features indicate that both concerted and sequential mechanisms are involved in the $Br^{2+} + C^+ + N^+$ and $Br^{3+} + C^+ + N^+$ channels. For the sequential mechanism, only the CN^{2+} that are the intermediates are observed. The sequential reaction pathways are further confirmed by the Newton diagrams. As shown in Figs. 8(b) and 8(c) for $Br^{2+} + C^+ + N^+$ and Figs. 8(f) and 8(g) for $Br^{3+} + C^+ + N^+$, respectively, the circular structures are observed only when Br^{2+} and Br^{3+} are the references. The native frame plots for $Br^{2+} + C^+ + N^+$ and for $Br^{3+} + C^+ + N^+$ are shown in Figs. 8(d) and 8(h), respectively. Conditions I and II mark the events from concerted and sequential fragmentations, respectively.

For the concerted mechanism, the Dalitz plots, Newton diagrams, and the KER distributions are shown in Figs. 9(a)–9(c) for the $Br^{2+} + C^+ + N^+$ channel and Figs. 9(d)–9(f) for the $Br^{3+} + C^+ + N^+$ channel, respectively. The peaks of the MCA between the N^+ ion and the Br^{2+} ion, and between N^+ and C^+, are 156°, and 64°, respectively, for the $Br^{2+} + C^+ + N^+$ channel. Correspondingly, the MCAs for the $Br^{3+} + C^+ + N^+$ channel are found to be 160°, and 56° between the N^+ ion and the Br^{3+}, and between the N^+ and C^+, respectively. With the increasing charge states of Br ions, the repulsions between Br ions and C^+, and those between Br ions and N^+ become stronger. As a result, the MCAs between the N^+ ions and the Br^{l+} ($l = 1$–3) ions and those between the C^+ ions and the Br^{l+} ($l = 1$–3) ions increase

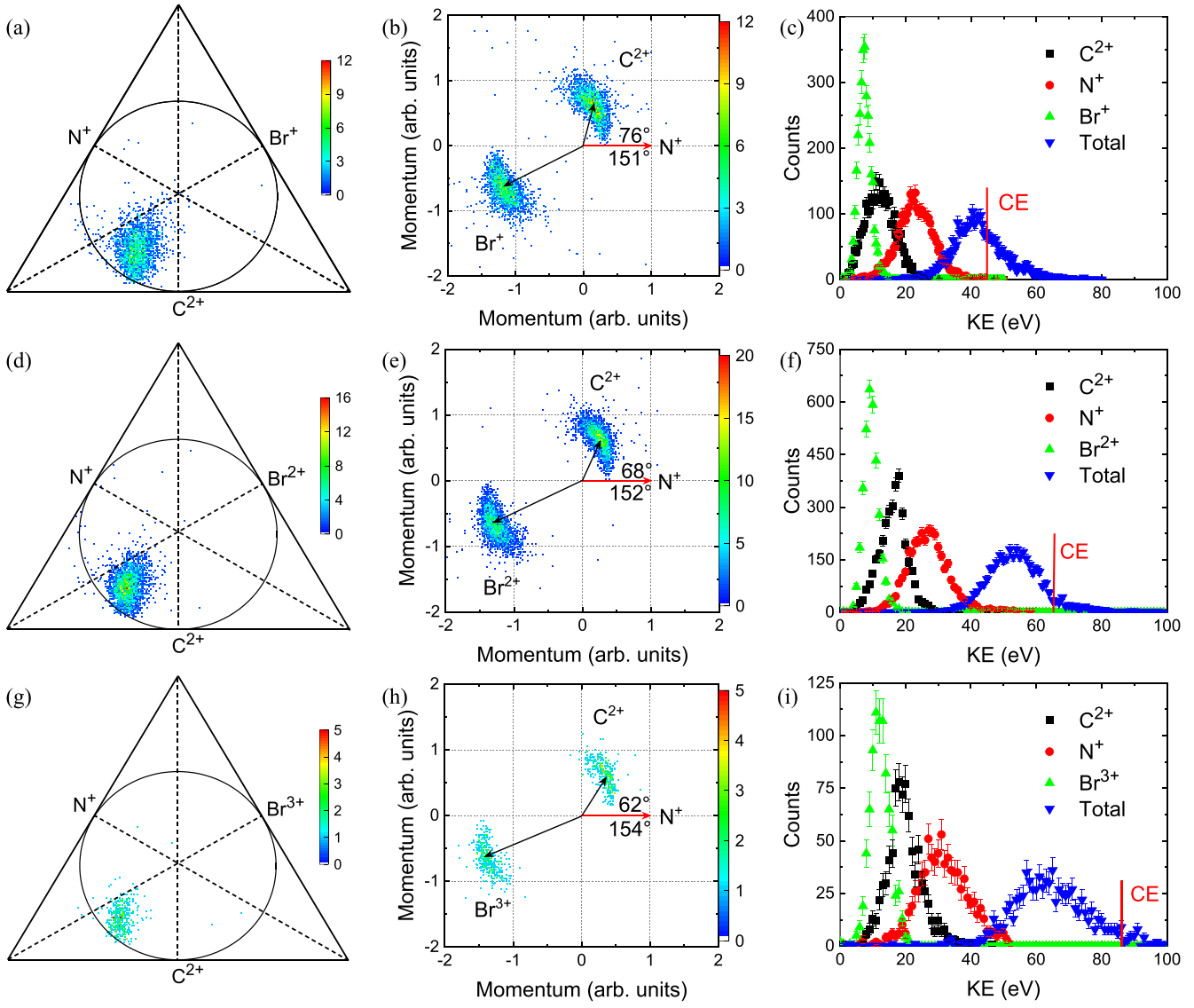

FIG. 10. Experimental results for the $Br^{l+} + C^{2+} + N^+$ ($l = 1$–3) channel. The Dalitz plots, Newton diagrams with N^+ as references, and KER distributions are shown in the first, second, and third columns, respectively. The angles on the upper and lower halves of the Newton diagrams are MCAs between the N ion and C ion, and those between the N ion and Br ions, respectively. Red solid lines in the right columns represent the KERs predicted by the CE model.

with the charge states. The KERs for the $Br^{2+} + C^+ + N^+$ and $Br^{3+} + C^+ + N^+$ channels extend from 20 to 50 eV with a peak at 33 eV and from 26 to 62 eV with the most probable value at 43 eV, respectively.

The Dalitz plot, Newton diagram, and KER distribution for sequential dissociation of the $Br^{2+} + C^+ + N^+$ channel are displayed in Figs. 9(g)–9(i). In Fig. 8(d), the window condition does not include the full angles to avoid overlap between sequential and concerted mechanisms; only a half-circular structure in the Newton diagram is presented. Still, this is clear evidence of the sequential mechanism. The KER distribution ranges from about 21 to 40 eV with the most probable value at about 28 eV and that in the first step extends from about 12 to 30 eV with a peak value of about 21.5 eV. The KER distribution of the second step, i.e., $CN^{2+} \rightarrow C^+ + N^+$, ranges from 2 to 13 eV with the most probable value of 6.5 eV, which agrees with the result of the second step of the sequential dissociation process of the $BrCN^{3+} \rightarrow Br^+ + CN^{2+} \rightarrow Br^+ + C^+ + N^+$ channel, as shown in Fig. 7(f). As compared in region II of Figs. 8(d) and 8(h), the KERs of CN^{2+} from the $Br^{2+} + C^+ + N^+$ and $Br^{3+} + C^+ + N^+$ channels are in the same range. The branching ratios of the concerted and the sequential processes for the $Br^{2+} + C^+ + N^+$ channel are $96.3\% \pm 2\%$ and $3.7\% \pm 2\%$, respectively. For the sequential fragmentation of the $Br^{3+} + C^+ + N^+$ channel, the counts are quite limited, as marked in Fig. 8(h), which are not discussed in this work. The most probable value, maximum value, and width of KER for the concerted and sequential

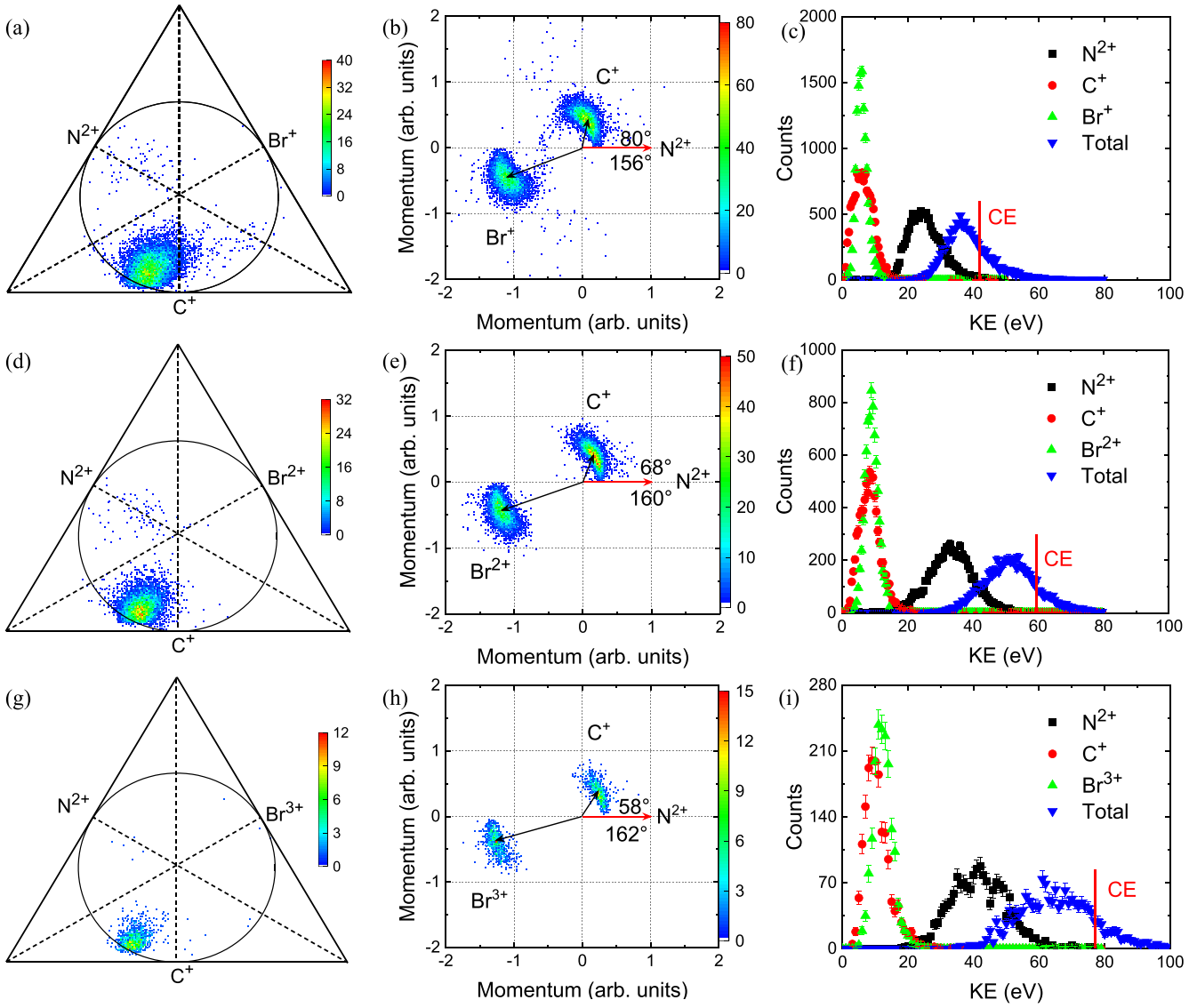

FIG. 11. Experimental results for the $Br^{l+} + C^+ + N^{2+}$ (l = 1–3) channel. The Dalitz plots, Newton diagrams with N^{2+} as references, and KER distributions are shown in the first, second, and third columns, respectively. The angles on the upper and lower halves of the Newton diagrams are MCAs between the N ion and C ion, and those between the N ion and Br ions, respectively. Red solid lines in the right column represent the KERs predicted by the CE model.

processes of the $Br^{l+} + C^+ + N^+$ (l = 1–3) channel are listed in Table II.

C. Concerted fragmentation dynamics of $Br^{l+} + C^{2+} + N^+$, $Br^{l+} + C^+ + N^{2+}$ (l = 1–3), $Br^+ + C^{2+} + N^{2+}$, and $Br^{2+} + C^{2+} + N^{2+}$ channels

Figures 10(a)–10(c), 10(d)–10(f), and 10(g)–10(i) display the Dalitz plot, Newton diagram, and the kinetic energy distribution of the $Br^{l+} + C^{2+} + N^+$ channels for l = 1, 2, and 3, respectively. Figure 11 shows the same plots as Fig. 10 for the $Br^{l+} + C^+ + N^{2+}$ (l = 1–3) channels. The same plots of the $Br^+ + C^{2+} + N^{2+}$ and $Br^{2+} + C^{2+} + N^{2+}$ channels are shown in the first and second rows of Fig. 12, respectively. For all of the aforementioned channels, the features in the Dalitz and Newton plots indicate that only the concerted mechanism is observed. Similar to the $Br^{l+} + C^+ + N^+$ (l = 1–3) channel, the Coulomb repulsion between the ions increases with the charge states of the bromine ion. As a result, the MCAs between bromine and carbon ions, and that between bromine and nitrogen ions increase as a function of the charge states, as shown in the middle columns of Figs. 10 –12. The experimental KERs present Gaussian profiles and the peak values increase with the charge states of the bromine ion for specific carbon and nitrogen charge states, as shown in the right columns of Figs. 10–12.

D. Discussion

For all of the sequential fragmentation channels, $BrCN^{3+} \rightarrow Br^+ + CN^{2+} \rightarrow Br^+ + C^+ + N^+$, $BrCN^{3+} \rightarrow BrC^{2+} + N^+ \rightarrow Br^+ + C^+ + N^+$, and $BrCN^{4+} \rightarrow Br^{2+} + CN^+ \rightarrow Br^{2+} + C^+ + N^+$, the peaks of the KERs are lower than those of the corresponding concerted mechanism.

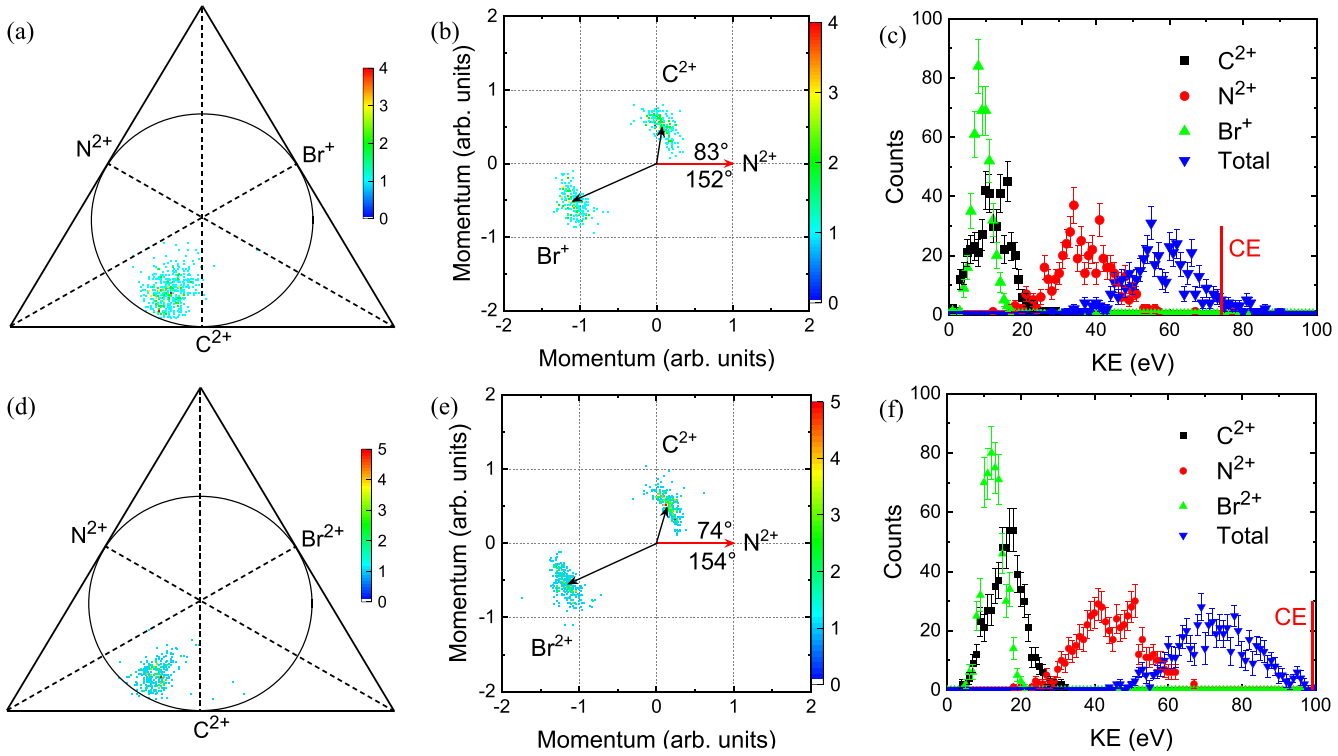

FIG. 12. Experimental results for the $Br^{l+} + C^{2+} + N^{2+}$ (l = 1–2) channel. The Dalitz plots, Newton diagrams with N^{2+} as references, and KER distributions are shown in the first, second, and third columns, respectively. The angles on the upper and lower halves of the Newton diagrams are MCAs between the N ion and C ion, and those between the N ion and Br ions, respectively. Red solid lines in the right column represent the KERs predicted by the CE model.

This means all of the sequential channels originate from the lower-lying electronic states. The KER differences between the sequential fragmentations of $BrCN^{3+}$ and $BrCN^{4+}$ almost come from the first step dissociation, as shown in Figs. 7(f), 7(i), and 9(i). As aforementioned, the second step dissociations $CN^{2+} \rightarrow C^+ + N^+$ from both $BrCN^{3+}$ and $BrCN^{4+}$ give almost identical KERs indicating that the same electronic states are involved. For the $BrCN^{3+} \rightarrow BrC^{2+} + N^+ \rightarrow Br^+ + C^+ + N^+$ channel, the KER of the second step, $BrC^{2+} \rightarrow Br^+ + C^+$, is lower than the other channels. This is because the bond length of Br-C (1.79 Å) is larger than the C-N bond (1.16 Å) at the equilibrium geometry of BrCN. For the charged state of the molecule, the bond length of intermediate BrC^{2+} may also be larger than that of CN^{2+}, leading to lower KER.

As for the concerted fragmentation channels in this work, the momenta of nitrogen are always smaller than that of the bromine ion. This is due to the fact that the mass of bromine is much heavier than carbon and nitrogen. At the beginning of the Coulomb explosion, the bromine ion is almost at rest and the shorter bond length of C-N leads to a strong repulsion force between carbon and nitrogen ions. The repulsion between carbon and nitrogen ions pushes carbon to come close to the bromine since the mass of carbon is lighter than nitrogen. In this case, the internuclear distance between bromine and carbon decreases first which can be even much shorter than the initial bond length of C-N. As a result, the momenta of the bromine ion could be larger than that of nitrogen.

As for the KERs predicted by the Coulomb explosion model, they deviated from the experimental peaks for the channels with charge states $\geqslant$5, e.g., $Br^{3+} + C^+ + N^+$, $Br^{2+} + C^{2+} + N^+$, $Br^{2+} + C^+ + N^{2+}$, $Br^+ + C^{2+} + N^{2+}$, $Br^{3+} + C^{2+} + N^+$, $Br^{3+} + C^+ + N^{2+}$, and $Br^{2+} + C^{2+} + N^{2+}$, where some of the predicated KERs are out of the experimental range. Even for the other channels with charge states $\leqslant$4, the KERs obtained from the Coulomb explosion model are still higher than the peak of the experiment. The reason for the deviations may be the charge rearrangement at the very beginning of the dissociation. For the multiple

TABLE II. The most probable value and range of KER for the concerted and sequential processes of the the $Br^{l+} + C^+ + N^+$ (l = 1–3) channel.

Channels	Most probable KER (eV)	Range of KER (eV)
$BrCN^{3+} \rightarrow Br^+ + C^+ + N^+$	20.5	13–35
$BrCN^{3+} \rightarrow Br^+ + CN^{2+}$	19	13–27
$\rightarrow Br^+ + C^+ + N^+$		
$BrCN^{3+} \rightarrow N^+ + BrC^{2+}$	17.5	12–25
$\rightarrow Br^+ + C^+ + N^+$		
$BrCN^{4+} \rightarrow Br^{2+} + C^+ + N^+$	33	20–50
$BrCN^{4+} \rightarrow Br^{2+} + CN^{2+}$	28	21–40
$\rightarrow Br^{2+} + C^+ + N^+$		
$BrCN^{5+} \rightarrow Br^{3+} + C^+ + N^+$	43	26–62

ionization of molecules by electron impact, the most probable mechanism could be the inner shell ionization, following Meitner-Auger decay [68]. The heavier element has a higher inner valence ionization cross section than the light element. Hence, the positive charges are localized on the bromine ions after the local Meitner-Auger decay. For the more highly charged state, the Br-C chemical bond is broken and dissociates very fast. Simultaneously, there is electron transfer from the CN group to the bromine ion which can occur within a very long Br-C internuclear distance due to the highly charged state of bromine. As a result, the effective internuclear distance of the Coulomb explosion of the highly charged state is larger than the equilibrium geometry and a lower experimental KER can be expected. The internuclear distance for electron transfer can be estimated by the classical over-the-barrier model [69,70]. The predicted internuclear distances for electron transfer from carbon (here, we take neutral carbon, ionization potential IP = 11.26 eV [71], for an example) to Br^{4+}, Br^{5+}, and Br^{6+} are 6.4, 7.0, and 7.5 Å, which are much larger than the equilibrium bond length of C-Br (1.79 Å) [72].

IV. CONCLUSION

In conclusion, the fragmentation dynamics of the $BrCN^{q+}$ ($q = 3$–6) induced by 1-keV electrons was studied employing the ion momentum imaging technique. Eleven three-body fragmentation channels were identified and their KER distributions are obtained. The fragmentation mechanisms for these channels were studied with the help of Dalitz plots, Newton diagrams, and native frame methods. The sequential fragmentation processes were observed in the following channels: $BrCN^{3+} \rightarrow N^+ + BrC^{2+} \rightarrow Br^+ + C^+ + N^+$, $BrCN^{3+} \rightarrow Br^+ + CN^{2+} \rightarrow Br^+ + C^+ + N^+$, $BrCN^{4+} \rightarrow Br^{2+} + CN^{2+} \rightarrow Br^+ + C^+ + N^+$, and $BrCN^{5+} \rightarrow Br^{3+} + CN^{2+} \rightarrow Br^+ + C^+ + N^+$, and the concerted fragmentation processes exist in all 11 channels. For the concerted fragmentation of all the channels, the experimental KERs are lower than the predictions by the Coulomb explosion model. The reason is ascribed to the ultrafast dissociation and electron transfer at the very beginning of the dissociation which results in a prolonged internuclear distance compared to the equilibrium geometry.

ACKNOWLEDGMENTS

This work is supported by the National Key Research and Development Program of China (Grant No. 2022YFA1602502), the National Natural Science Foundation of China (Grant No. 12204454), the Strategic Priority Research Program of Chinese Academy of Sciences (Grant No. XDB34020000), the CAS Pioneer Hundred Talents Program, and the USTC Research Funds of the Double First-Class Initiative.

[1] J. Lilensten, C. S. Wedlund, M. Barthélémy, R. Thissen, D. Ehrenreich, G. Gronof, and O. Witasse, Icarus **222**, 169 (2013).
[2] R. Thissen, O. Witasse, O. Dutuit, C. S. Wedlund, G. Gronoff, and J. Lilensten, Phys. Chem. Chem. Phys. **13**, 18264 (2011).
[3] G. L. Rogoff, J. M. Kramer, and R. B. Piejak, IEEE Trans. Plasma Sci. **14**, 103 (1986).
[4] P. L. G. Ventzek, M. Grapperhaus, and M. J. Kushner, J. Vac. Sci. Technol. B **12**, 3118 (1994).
[5] M. J. Kushner, J. Appl. Phys. **82**, 5312 (1997).
[6] D. Reiter and R. K. Janev, Contrib. Plasm. Phys. **50**, 986 (2010).
[7] B. Boudaïffa, P. Cloutier, D. Hunting, M. A. Huels, and L. Sanche, Science **287**, 1658 (2000).
[8] P. López-Tarifa, M. A. Hervé du Penhoat, R. Vuilleumier, M. P. Gaigeot, I. Tavernelli, A. Le Padellec, J. P. Champeaux, M. Alcamí, P. Moretto-Capelle, F. Martín, and M. F. Politis, Phys. Rev. Lett. **107**, 023202 (2011).
[9] P. López-Tarifa, M. P. Gaigeot, R. Vuilleumier, I. Tavernelli, M. Alcamí, F. Martín, M. A. Hervé Du Penhoat, and M. F. Politis, Angew. Chem. Int. Ed. **52**, 3160 (2013).
[10] S. Maclot, D. G. Piekarski, A. Domaracka, A. Méry, V. Vizcaino, L. Adoui, F. Martín, M. Alcamí, B. A. Huber, P. Rousseau, and S. Díaz-Tendero, J. Phys. Chem. Lett. **4**, 3903 (2013).
[11] X. Ren, T. Pflüger, M. Weyland, W. Y. Baek, H. Rabus, J. Ullrich, and A. Dorn, J. Chem. Phys. **141**, 134314 (2014).
[12] K. Nagaya, K. Motomura, E. Kukk, H. Fukuzawa, S. Wada, T. Tachibana, Y. Ito, S. Mondal, T. Sakai, K. Matsunami, R. Koga, S. Ohmura, Y. Takahashi, M. Kanno, A. Rudenko, C. Nicolas, X.-J. Liu, Y. Zhang, J. Chen, M. Anand *et al.*, Phys. Rev. X **6**, 021035 (2016).
[13] X. Ren, E. Wang, A. D. Skitnevskaya, A. B. Trofimov, K. Gokhberg, and A. Dorn, Nat. Phys. **14**, 1062 (2018).
[14] S. Xu, D. Guo, X. Ma, X. Zhu, W. Feng, S. Yan, D. Zhao, Y. Gao, S. Zhang, X. Ren, Y. Zhao, Z. Xu, A. Dorn, L. S. Cederbaum, and N. V. Kryzhevoi, Angew. Chem. Int. Ed. **57**, 17023 (2018).
[15] T. Masuoka and I. Koyano, J. Chem. Phys. **95**, 909 (1991).
[16] S. Hsieh and J. H. D. Eland, J. Phys. B: At., Mol. Opt. Phys. **30**, 4515 (1997).
[17] S. Falcinelli, M. Rosi, P. Candori, F. Vecchiocattivi, J. M. Farrar, F. Pirani, N. Balucani, M. Alagia, R. Richter, and S. Stranges, Planet. Space Sci. **99**, 149 (2014).
[18] K. Codling, L. J. Frasinskit, P. A. Hatherlyt, M. Stankiewiczt, and F. P. Larkins, J. Phys. B: At., Mol. Opt. Phys. **24**, 951 (1991).
[19] N. Saito, M. Nagoshi, M. Machida, I. Koyano, A. De Fanis, and K. Ueda, Chem. Phys. Lett. **393**, 295 (2004).
[20] R. Singh, P. Bhatt, N. Yadav, and R. Shanker, Phys. Rev. A **87**, 022709 (2013).
[21] T. Pflüger, X. Ren, and A. Dorn, Phys. Rev. A **91**, 052701 (2015).
[22] Z. Shen, E. Wang, M. Gong, X. Shan, and X. Chen, J. Chem. Phys. **145**, 234303 (2016).
[23] E. Wang, M. Gong, Z. Shen, X. Shan, X. Ren, A. Dorn, and X. Chen, J. Chem. Phys. **149**, 204301 (2018).
[24] L. Chen, X. Shan, E. Wang, X. Ren, X. Zhao, W. Huang, and X. Chen, Phys. Rev. A **100**, 062707 (2019).
[25] L. Adoui, M. Tarisien, J. Rangama, P. Sobocinsky, A. Cassimi, J.-Y. Chesnel, F. Frémont, B. Gervais, A. Dubois, M. Krishnamurthy, S. Kumar, and D. Mathur, Phys. Scr. **T92**, 89 (2001).

[26] N. Neumann, D. Hant, L. P. H. Schmidt, J. Titze, T. Jahnke, A. Czasch, M. S. Schöffler, K. Kreidi, O. Jagutzki, H. Schmidt-Böcking, and R. Dörner, Phys. Rev. Lett. **104**, 103201 (2010).

[27] S. Xu, X. L. Zhu, W. T. Feng, D. L. Guo, Q. Zhao, S. Yan, P. Zhang, D. M. Zhao, Y. Gao, S. F. Zhang, J. Yang, and X. Ma, Phys. Rev. A **97**, 062701 (2018).

[28] Y. Zhang, T. Jiang, L. Wei, D. Luo, X. Wang, W. Yu, R. Hutton, Y. Zou, and B. Wei, Phys. Rev. A **97**, 022703 (2018).

[29] L. Chen, X. Shan, X. Zhao, X. Zhu, X. Hu, Y. Wu, W. Feng, D. Guo, R. Zhang, Y. Gao, Z. Huang, J. Wang, X. Ma, and X. Chen, Phys. Rev. A **99**, 012710 (2019).

[30] X. Zhao, X. Shan, X. Zhu, L. Chen, Z. Shen, W. Feng, D. Guo, D. Zhao, R. Zhang, Y. Gao, Z. Huang, S. Zhang, X. Ma, and X. Chen, Phys. Rev. A **103**, 012802 (2021).

[31] B. Wang, J. Han, X. Zhu, L. Wei, B. Ren, Y. Zhang, W. Yu, S. Yan, X. Ma, Y. Zou, L. Chen, and B. Wei, Phys. Rev. A **103**, 042810 (2021).

[32] H. Yuan, Z. Xu, S. Xu, C. Ma, Z. Zhang, D. Guo, X. Zhu, D. Zhao, S. Zhang, S. Yan, Y. Gao, R. Zhang, and X. Ma, Phys. Rev. A **105**, 022814 (2022).

[33] Z. He, J. Wang, Y. Zhang, B. Wang, J. Han, B. Ren, L. Wei, Z. Xia, P. Ma, T. Meng, Y. Zou, Z. Hu, and B. Wei, Phys. Rev. A **105**, 022818 (2022).

[34] B. Ren, P. Ma, Y. Zhang, L. Wei, J. Han, Z. Xia, J. Wang, T. Meng, W. Yu, Y. Zou, C.-L. Yang, and B. Wei, Phys. Rev. A **106**, 012805 (2022).

[35] C. Wu, C. Wu, D. Song, H. Su, X. Xie, M. Li, Y. Deng, Y. Liu, and Q. Gong, J. Chem. Phys. **140**, 141101 (2014).

[36] X. Gong, M. Kunitski, L. Ph. H. Schmidt, T. Jahnke, A. Czasch, R. Dörner, and J. Wu, Phys. Rev. A **88**, 013422 (2013).

[37] J. Zhou, C. He, M. Liu, E. Wang, S. Jia, A. Dorn, X. Ren, and Y. Liu, Phys. Rev. Res. **3**, 023050 (2021).

[38] B. Jochim, M. Zohrabi, B. Gaire, F. Anis, T. Uhlíková, K. D. Carnes, E. Wells, B. D. Esry, and I. Ben-Itzhak, Phys. Rev. A **105**, 043101 (2022).

[39] T. Severt, D. R. Daugaard, T. Townsend, F. Ziaee, K. Borne, S. Bhattacharyya, K. D. Carnes, D. Rolles, A. Rudenko, E. Wells, and I. Ben-Itzhak, Phys. Rev. A **105**, 053112 (2022).

[40] L. Adoui, T. Muranaka, M. Tarisien, S. Legendre, G. Laurent, A. Cassimi, J.-Y. Chesnel, X. Fléchard, F. Frémont, B. Gervais, E. Giglio, and D. Hennecart, Nucl. Instrum. Methods Phys. Res. Sect. B **245**, 94 (2006).

[41] E. Wang, X. Shan, Y. Shi, Y. Tang, and X. Chen, Rev. Sci. Instrum. **84**, 123110 (2013).

[42] A. Khan, L. C. Tribedi, and D. Misra, Rev. Sci. Instrum. **86**, 043105 (2015).

[43] J. Ullrich, R. Moshammer, A. Dorn, R. Dörner, L. P. H. Schmidt, and H. Schmidt-Böcking, Rep. Prog. Phys. **66**, 1463 (2003).

[44] H. Schmidt-Böcking, M. S. Schöffer, T. Jahnke, A. Czasch, V. Mergel, L. Schmidt, R. Dörner, O. Jagutzki, M. Hattass, Th. Weber, E. Weigold, H. T. Schmidt, R. Schuch, H. Cederquist, Y. Demkov, C. Whelan, A. Gudonov, and J. Walters, Nucl. Instrum. Methods Phys. Res. Sect. B **233**, 3 (2005).

[45] R. Dörner, V. Mergel, L. Spielberger, O. Jagutzki, M. Unverzagt, W. Schmitt, J. Ullrich, R. Moshammer, H. Khemliche, M. Prior, R. E. Olson,L. Zhaoyuan, W. Wu, C. L. Cocke, and H. Schmidt-Böcking, in *The 19th International Conference on the Physics of Electronic and Atomic Collisions*, AIP Conf. Proc. No. 360 (AIP, Melville, NY, 1996), p. 495.

[46] U. Ablikim, C. Bomme, T. Osipov, H. Xiong, R. Obaid, R. C. Bilodeau, N. G. Kling, I. Dumitriu, S. Augustin, S. Pathak, K. Schnorr, D. Kilcoyne, N. Berrah, and D. Rolles, Rev. Sci. Instrum. **90**, 055103 (2019).

[47] R. H. Dalitz, Philos. Mag. **44**, 1068 (1953).

[48] R. H. Dalitz, Phys. Rev. **94**, 1046 (1954).

[49] J. Rajput, T. Severt, B. Berry, B. Jochim, P. Feizollah, B. Kaderiya, M. Zohrabi, U. Ablikim, F. Ziaee, K. Raju P., D. Rolles, A. Rudenko, K. D. Carnes, B. D. Esry, and I. Ben-Itzhak, Phys. Rev. Lett. **120**, 103001 (2018).

[50] H. Kumar, P. Bhatt, C. P. Safvan, and J. Rajput, J. Chem. Phys. **148**, 064302 (2018).

[51] C. Wu, C. Wu, D. Song, H. Su, Y. Yang, Z. Wu, X. Liu, H. Liu, M. Li, Y. Deng, Y. Liu, L.-Y. Peng, H. Jiang, and Q. Gong, Phys. Rev. Lett. **110**, 103601 (2013).

[52] A. Khan, L. C. Tribedi, and D. Misra, Phys. Rev. A **92**, 030701(R) (2015).

[53] E. Wang, X. Shan, Z. Shen, M. Gong, Y. Tang, Y. Pan, K.-C. Lau, and X. Chen, Phys. Rev. A **91**, 052711 (2015).

[54] E. Wang, X. Shan, Z. Shen, X. Li, M. Gong, Y. Tang, and X. Chen, Phys. Rev. A **92**, 062713 (2015).

[55] R. Singh, P. Bhatt, N. Yadav, and R. Shanker, J. Phys. B: At. Mol. Phys. **46**, 085203 (2013).

[56] P. Bhatt, R. Singh, N. Yadav, and R. Shanker, Phys. Rev. A **86**, 052708 (2012).

[57] A. Khan, L. C. Tribedi, and D. Misra, Phys. Rev. A **96**, 012703 (2017).

[58] J. Roberts, S. Wang, P. Veres, J. A. Neuman, H. Allen, J. Crounse, M. Kim, L. Xu, P. Wennberg, A. Rollins, I. Bourgeois, J. Peischl, T. Ryerson, and C. Thompson, Observations of cyanogen bromide (BrCN) in the global atmosphere during the NASA Atmospheric Tomography mission (ATom) and implications for active bromine chemistry, in *EGU General Assembly 2021* (2021), p. EGU21-7988.

[59] F. Brüning, I. Hahndorf, A. Stamatovic, and E. Illenberger, J. Phys. Chem. **100**, 19740 (1996).

[60] J. Royal and A. E. Orel, J. Chem. Phys. **125**, 214307 (2006).

[61] X. Gao, F. An, H. Li, J.-C. Xie, X.-D. Wang, X. Meng, B. Wu, D.-Q. Xie, and S. X. Tian, J. Phys. Chem. Lett. **11**, 9110 (2020).

[62] X.-F. Gao, H. Li, X. Meng, and S.-X. Tian, Chin. J. Chem. Phys. **32**, 89 (2019).

[63] S. Zhang, X. Wang, W. Jiang, Y. Zhang, Y. Jiang, and Z. Zhu, J. Chem. Phys. **156**, 134302 (2022).

[64] W. Jiang, X. Wang, S. Zhang, R. Dong, Y. Guo, J. Feng, Z. Shen, T. Yan, Z. Zhu, and Y. Jiang, J. Chem. Phys. **157**, 084302 (2022).

[65] L. Chen, E. Wang, W. Zhao, M. Gong, X. Shan, and X. Chen, J. Chem. Phys. **158**, 054301 (2023).

[66] V. Brites, Comput. Theor. Chem. **969**, 13 (2011).

[67] J. Fišer and R. Polák, Chem. Phys. **392**, 55 (2012).

[68] A. C. Thompson, D. T. Attwood, E. M. Gullikon, M. R. Howells, K.-J. Kim, J. Kirz, J. B. Kortright, I. Lindau, Y. Liu, P. Pianetta, A. L. Robinson, J. H. Scofield, J. H. Underwood, G. P. Williams, and H. Winick, *X-Ray Data Booklet* (Lawrence Berkeley National Laboratory, University of California Berkeley, 2009), pp. 1–3.

[69] K. Schnorr, A. Senftleben, M. Kurka, A. Rudenko, G. Schmid, T. Pfeifer, K. Meyer, M. Kübel, M. F. Kling, Y. H. Jiang, R. Treusch, S. Düsterer, B. Siemer, M. Wöstmann, H. Zacharias,

R. Mitzner, T. J. M. Zouros, J. Ullrich, C. D. Schröter, and R. Moshammer, Phys Rev. Lett. **113**, 073001 (2014).

[70] B. Erk, R. Boll, S. Trippel, D. Anielski, L. Foucar, B. Rudek, S. W. Epp, R. Coffee, S. Carron, S. Schorb, K. R. Ferguson, M. Swiggers, J. D. Bozek, M. Simon, T. Marchenko, J. Kupper, I. Schlichting, J. Ullrich, C. Bostedt, D. Rolles *et al.*, Science **345**, 288 (2014).

[71] S. G. Lias and J. F. Liebman, Ion energetics data, in *NIST Chemistry WebBook, NIST Standard Reference Database Number 69*, edited by P. J. Linstrom and W. G. Mallard (National Institute of Standards and Technology, Gaithersburg, MD, 2023), p. 20899, https://doi.org/10.18434/T4D303.

[72] I. Bhattacharyya, B. MondaL, N. C. Bera, and A. K. Das, Int. J. Quantum Chem. **110**, 1165 (2010).